Microstructural evolution during thermal annealing of ice-Ih

Karoly Hidas, Andrea Tommasi, David Mainprice, Thomas Chauve, Fabrice Barou, Maurine Montagnat

▶ **To cite this version:**

Karoly Hidas, Andrea Tommasi, David Mainprice, Thomas Chauve, Fabrice Barou, et al.. Microstructural evolution during thermal annealing of ice-Ih. Journal of Structural Geology, 2017, 99, pp.31-44. 10.1016/j.jsg.2017.05.001 . hal-01685644

HAL Id: hal-01685644
https://hal.science/hal-01685644

Submitted on 2 Mar 2021

HAL is a multi-disciplinary open access archive for the deposit and dissemination of scientific research documents, whether they are published or not. The documents may come from teaching and research institutions in France or abroad, or from public or private research centers.

L'archive ouverte pluridisciplinaire **HAL**, est destinée au dépôt et à la diffusion de documents scientifiques de niveau recherche, publiés ou non, émanant des établissements d'enseignement et de recherche français ou étrangers, des laboratoires publics ou privés.

Distributed under a Creative Commons Attribution 4.0 International License

Microstructural evolution during thermal annealing of ice-I_h

Károly Hidas [a, *], Andréa Tommasi [a], David Mainprice [a], Thomas Chauve [b], Fabrice Barou [a], Maurine Montagnat [b]

[a] Géosciences Montpellier, CNRS & Université de Montpellier, Place E. Bataillon, 34095 cedex 5, Montpellier, France
[b] Institut des Géosciences de l'Environnement, Université Grenoble Alpes / CNRS, 54 rue Molière, BP96, 38402 cedex, Saint-Martin d'Hères, France

We studied the evolution of the microstructure of ice-I_h during static recrystallization by stepwise annealing experiments. We alternated thermal annealing and electron backscatter diffraction (EBSD) analyses on polycrystalline columnar ice pre-deformed in uniaxial compression at temperature of −7 °C to macroscopic strains of 3.0–5.2. Annealing experiments were carried out at −5 °C and −2 °C up to a maximum of 3.25 days, typically in 5–6 steps. EBSD crystal orientation maps obtained after each annealing step permit the description of microstructural changes. Decrease in average intragranular misorientation at the sample scale and modification of the misorientation across subgrain boundaries provide evidence for recovery from the earliest stages of annealing. This initial evolution is similar for all studied samples irrespective of their initial strain or annealing temperature. After an incubation period ≥1.5 h, recovery is accompanied by recrystallization (nucleation and grain boundary migration). Grain growth proceeds at the expense of domains with high intragranular misorientations, consuming first the most misorientated parts of primary grains. Grain growth kinetics fits the parabolic growth law with grain growth exponents in the range of 2.4–4.0. Deformation-induced tilt boundaries and kink bands may slow down grain boundary migration. They are stable features during early stages of static recrystallization, only erased by normal growth, which starts after >24 h of annealing.

1. Introduction

Unless exhumed rapidly due to tectonic processes, rocks deformed in the middle crust and deeper in the Earth remain at high temperature for extended time spans after the cessation of deformation. This results in annealing of the deformation microstructure by a series of thermally activated, diffusion-based processes, namely: recovery and static recrystallization, which may also modify the crystal preferred orientation (CPO) or texture. Understanding the effects of annealing on the microstructure and CPO is therefore of utmost importance for the interpretation of the microstructures and for the estimation of the anisotropy of physical properties of lower crustal and mantle rocks.

In situ observations of the evolution of the microstructures and CPO during annealing enable the study of the interplay between the various physical processes involved in annealing (recovery, nucleation, grain growth). They also allow the analysis of the impact of the pre-existing deformation microstructures on the microstructural and CPO evolution during annealing. Numerous studies have dealt with annealing phenomena in metals and alloys (see Humphreys and Hatherly, 2004 for a review) and in situ static recrystallization has also been extensively studied in halite (Bestmann et al., 2005; Piazolo et al., 2006; Borthwick and Piazolo, 2010). However, most of these studies focused on cubic materials, which due to their high symmetry have a large number of possible slip systems with similar strengths and, hence, deform more homogeneously than most common minerals in the Earth crust and mantle. Here we present a study on ice-I_h – the typical form of water ice on the Earth's surface, with hexagonal crystal symmetry. Ice-I_h has a high viscoplastic anisotropy, since it deforms primarily by glide of dislocations on the basal plane (Duval et al., 1983). This high viscoplastic anisotropy induces a strong heterogeneity of stresses and strains at both the intra- and intergranular scales (Grennerat et al., 2012; Chauve et al., 2015), which results in onset of recrystallization at strains as low as 2% (Jacka, 1984; Chauve et al., 2015). This behavior makes ice-I_h an excellent analogue material for silicate minerals that compose the Earth.

* Corresponding author. Present address: Instituto Andaluz de Ciencias de la Tierra, CSIC & Universidad de Granada, Avenida de las Palmeras 4, 18100, Armilla, Granada, Spain.
E-mail address: karoly.hidas@gmail.com (K. Hidas).

Earlier studies of the annealing of ice-I_h focused on the evolution of CPO based on data of the orientation of crystallographic c-axes derived from optical imaging (*e.g.*, Steinemann, 1958; Rigsby, 1960; Jellinek and Gouda, 1969; Wilson, 1982; Ohotomo, 1985; Wilson et al., 2014; Peternell et al., 2014, Peternell and Wilson, 2016). These data do not allow the full characterization of the crystal orientation. As a consequence, misorientation gradients were not available to define sites with high geometrically necessary dislocation densities and, hence, high stored elastic energy, and the role of intra- and intergranular gradients in elastic energy on the annealing processes could not be evaluated. To investigate this question, we carried out stepwise annealing experiments on pre-deformed, laboratory-made polycrystalline columnar ice and analyzed the evolution of the microstructure after each annealing step using Electron Backscatter Diffraction (EBSD) data.

2. Materials and methods

2.1. Sample preparation

Rectangular-shaped, polycrystalline columnar ice specimens (Fig. 1a) with approximate dimensions of 90 × 90 × 15 mm and an average grain diameter of 10–15 mm in the plane normal to the columns' axis were produced in the Laboratoire de Glaciologie et Géophysique de l'Environnement (now Institut des Géosciences de l'Environnement, Grenoble, France) following the method of Plé and Meyssonnier (1997). The columnar grains have their [0001] axes normal (±15°) to the long axis of the columns (i.e., to the growth direction) (Fig. 1a). The specimens have therefore an initial weak CPO characterized by a girdle of [0001] subparallel to the sample surface.

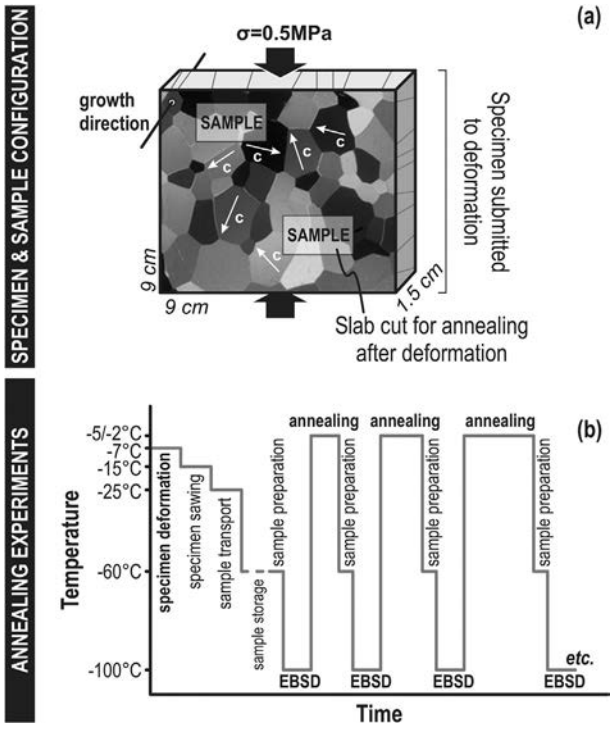

Fig. 1. (a) Schematic representation of the initial microstructure and experimental conditions for the creep test (modified from Montagnat et al., 2011) and of the sampling for annealing experiments. (b), Experimental conditions during deformation and stepwise annealing experiments. In (a), the white arrows on the sample surface show the theoretical c-axes orientation distribution of columnar ice crystals and wide black arrows indicate the compression direction. EBSD: crystal orientation measurements by electron backscatter diffraction.

These specimens were submitted to constant load uniaxial compression deformation experiments at the LGGE, using a mechanical press with a lever arm (see Montagnat et al., 2011 for more details). The experiments are run in a cold room at −7 °C (±0.5 °C) by applying a constant stress of 0.5 MPa normal to the long axes of the columnar crystals (Fig. 1a) until the specimens reached 3.0% (specimen CI06), 3.7% (specimen CI02), or 5.2% (specimen CI18) plastic strain, respectively. Note that analysis of deformation experiments of polycrystalline ice-I_h performed under similar temperature and stress conditions shows non-steady state deformation and incomplete grain size reduction up to strains of *ca.* 6% (*e.g.*, Montagnat et al., 2015).

Previous experiments show that annealing is very active in the first hours after unloading (*e.g.*, Peternell et al., 2014, Peternell and Wilson, 2016). To avoid as much non-controlled microstructural evolution as possible, the specimens were cooled to −15 °C within less than 15 min after unloading, and subsequent specimen preparation, transport, storage, and EBSD analysis were performed at this or substantially lower temperatures (Fig. 1b; see details below). However, upon unloading a creep experiment, polycrystalline ice shows recoverable strain due to the relaxation of the internal stress field by back motion of dislocations in pile-up configurations (Duval et al., 1983). In polycrystalline columnar ice similar to samples studied here, Grennerat et al. (2012) observed recoverable strains of up to 0.3% within a few minutes after unloading. This subtle relaxation, which certainly influence the dislocation fields and the stored energy, however, cannot be avoided. The remaining dislocations are mostly geometrically-necessary dislocations (*e.g.*, Ashby, 1970).

Deformed specimens were cut into several, approximately 2 × 1 cm sized slabs – usually containing less than 25 grains (Fig. 1a) – using a diamond saw in a cold room at −15 °C. Hereafter we will refer to these slabs as samples and, for the sake of simplicity, we will specify deformation and annealing conditions in square brackets each time a sample number appears in the text. For example, the notation "CI18Z6 [5.2/-2]" refers to the slab Z6 cut out from the specimen CI18 deformed to 5.2% and submitted to thermal annealing at −2 °C. The frozen samples were shipped to Montpellier in insulated containers at −25 °C, where they were stored at −60 °C (±1 °C) in a Labologic ultra-low temperature freezer in air-tight bags to minimize sublimation.

2.2. Electron backscatter diffraction (EBSD) analyses

For EBSD analysis, each sample was placed on a Gatan copper holder using thermally conductive silicone grease and then frozen onto the holder by injecting water around its edges. Sample preparation was achieved by scraping the surface with disposable Leica microtome blades, following the method of Piazolo et al. (2008). EBSD was performed at −100 °C (±5 °C) using a Gatan liquid nitrogen gas cooling cryogenic stage in the CamScan Crystal Probe X500-FEG SEM-EBSD facility of Géosciences Montpellier (Montpellier, France), which is equipped with Oxford Instruments NordlysNano EBSD detector and Aztec2.4 data acquisition software (Oxford/HKL). Instrumental settings were 15 kV acceleration voltage, 25 mm working distance, and 1 Pa chamber pressure. Acquisition conditions were 4 × 4 binning and low gain with grid steps of 20 μm for overview maps and 5 μm for high-resolution crystal orientation maps. Large area mapping was carried out by combined beam and stage scanning, hence the overview maps are mosaics of smaller maps. Percentage of indexed points in raw maps always exceeded 90%. Post-acquisition data treatment was carried out using the Channel5 algorithms by (1) removing isolated wild spikes, (2) filling the non-indexed pixels that have up to eight

identical neighbors with the same orientation and repeating this iterative operation using seven and six identical neighbors, and (3) removing grains defined by less than 10 indexed pixels.

For treating and visualizing EBSD data, we used the built-in functions of the MTEX4 Matlab toolbox (https://mtex-toolbox.github.io/; Bachmann et al., 2010). For grain recognition, we applied a segmentation angle (*i.e.*, a minimum threshold misorientation between neighboring pixels that defines a high-angle grain boundary) of 7° following Chauve et al. (2017), except for sample CI18Z6 [5.2/-2]. For this sample, due to the very close initial orientation of the parent grains, the fast multiscale clustering (FMC; McMahon et al., 2013) algorithm with C_{Maha} value − which is a constant scaling factor applied on Mahalanobis distance that controls segmentation sensitivity − in the range of 0.3−0.4 provided more reliable boundary definition than the segmentation method with a threshold of 7°.

2.3. Stepwise annealing experiments

Conducting in-situ annealing experiments in the SEM sample chamber is not possible due to rapid sublimation of ice at temperatures higher than *ca.* −50 °C at the pressure conditions <5 Pa required for EBSD measurements (Weikusat et al., 2011). We alternated therefore ex-situ annealing experiments in a Labologic high-precision laboratory freezer at −5 °C or at −2 °C (±0.1 °C) (0.98−0.99 T_m) at ambient pressure and EBSD analyses at −100 °C to avoid sublimation or microstructural changes during data acquisition (Fig. 1b). Despite annealing temperatures close to the melting point, we have not observed any evidence of melt at grain boundaries or in triple junctions. The first EBSD analyses were performed after 30 min or 1 h of annealing, and then the same area was reanalyzed again after 1.5 h, 2 h, 3 h, etc. up to *ca.* 24 h of cumulative annealing, except for one CI18Z6 [5.2/-2] for which we performed a longer annealing of 78 h (Table 1). A typical experiment consisted of 4−6 annealing steps with progressively longer annealing periods. The duration of the annealing steps was varied between the different experiments to test for a possible effect of the stepwise procedure (Table 1). Based on the absence of characteristic deviations in the microstructural evolution among the experiments interrupted at different annealing times and continued textural evolution on the same sites in consecutive annealing steps (cf. Results), we conclude that stepwise procedure has no major effect on the microstructural evolution during annealing.

Preparing the sample surface was necessary after each annealing step (Fig. 1b). The thickness of the surface layer removed during this preparation step ranged from 30 to 100 μm, as controlled by analyzing the change in focus values (Z) at the constant working distance in the SEM. The total thickness of the removed layer for a complete annealing experiment never exceeded 500 μm with respect to the deformed state at t_0. Note that due to the centimetric initial grain sizes and the "2D" geometry of the polycrystalline columnar ice, the initial grains (which became deformed porphyroclasts after the deformation experiments) crosscut the whole sample thickness. This "2D" geometry cannot be ensured for the recrystallized grains formed during the deformation experiments and, eventually, during annealing. However, the analysis of the EBSD maps indicates that most recrystallized grains attain millimetric sizes and that the microstructural evolution can be reliably followed between the different annealing experiments. To evaluate the possible effect of sample preparation on the microstructural evolution we carried out a control experiment, where no heating was applied between the EBSD analyses (Supplementary Fig. S1). This control experiment demonstrates that the bias on the microstructure characterization due to sample preparation is negligible in absence of heating. Nevertheless, to mitigate the 3D effect of sample preparation, we applied a minimum threshold of 30 min between two consecutive annealing steps. The volume loss due to preparation of the sample surface hinders, however, the quantitative measurement of grain-boundary migration rates. A minor advantage of the destructive sample preparation is the removal of the outermost surface layer, which may be damaged by thermal grooving and hence may slow boundary migration (Gottstein and Shvindlerman, 1992; Humphreys et al., 1996; Nakamichi et al., 2008). Recent comparison between 2D EBSD and 3D X-ray diffraction data for in-situ annealing experiments on halite corroborates that absolute grain boundary migration rates are significantly slower at the surface, but shows that relative mobility between boundaries with different structures are similar (Borthwick et al., 2012).

2.4. Characterization tools for the interpretation and graphical illustration of EBSD data

During the creep of ice, distortions in the crystal structure are accommodated by the formation of geometrically necessary dislocations (see Schulson and Duval., 2009 for a review). By using the intragranular misorientation gradients measured by EBSD as proxies for the geometrically necessary dislocation density and, hence of the stored elastic energy, we may therefore investigate the relationship between the local recrystallization kinetics and the local stored energy. Several methods have been proposed for characterizing misorientation gradients (see Wright et al., 2011 for a review). In the present study, we characterize intragranular misorientations by the misorientation relative to the mean orientation of a grain (Mis2Mean), which is the deviation in orientation at a measurement point from the mean orientation of the grain to which the point belongs. The spread in orientations within a grain is characterized by the grain orientation spread (GOS), which is the average of the Mis2Mean over the grain. Sharp gradients in misorientations, such as subgrain boundaries, are best visualized by calculating second nearest-neighbor Kernel Average Misorientations (2nd order KAM, hereafter KAM2) maps. The KAM2 is the deviation in orientation of a measurement pixel from the average orientation of its nearest 12 neighbors. Here it is calculated

Table 1
Summary of the experiments showing the temperature and achieved macroscopic strain of deformation against the conditions used for stepwise annealing experiments.

Deformation		Annealing			
Temperature	Strain	−5 °C		−2 °C	
		Sample	Total annealing time	Sample	Total annealing time
−7 °C	3.0%	CI06-Z2	0-1-2-3-5 h	CI06-Z10	0-0.5-1.5-3-5 h
	3.7%	CI02-Z1	0-1-2-3-4-6 h		
		CI02-Z4	0-1-2-3-4-6-25 h		
		CI02-Z9	0-0.5-2-4 h		
	5.2%	CI18-Z1	0-1-2-4.5-9-16-23 h	CI18-Z6	0-0.5-1.5-3-5-15-78 h

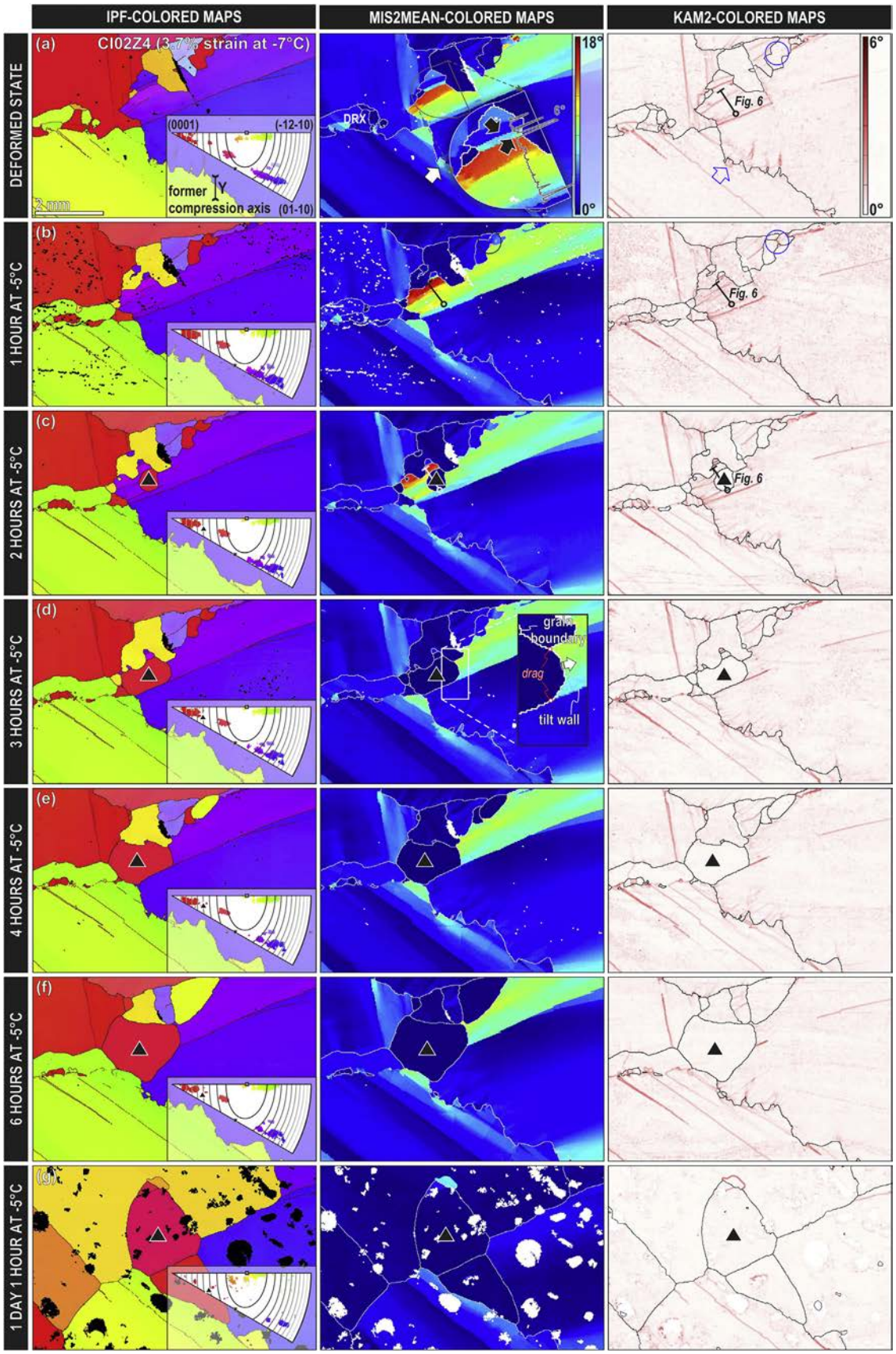

Fig. 2. Microstructural evolution during annealing at −5 °C of the sample CI02Z4, which was pre-deformed to 3.7% macroscopic strain at −7 °C. The same area is presented in all images. Left column: Crystal Preferred Orientation (CPO) maps for ice, color-coded with respect to the orientation of the former compression axis (Y) in the crystal reference frame. Inverse pole figure (IPF) is shown in the inset at the bottom-right corner of each map, legend is the same as for the deformed state. Contours in the IPF show Schmid factors from

with a cut-off value of 7° (segmentation angle used for defining a high angle boundary). To quantify the sinuosity of grain boundaries we use the PARIS factor (Percentile Average Relative Indented Surface; Panozzo and Hurlimann, 1983). Fully convex shapes have PARIS factors of 0% and this factor is not sensitive to the overall shape of the grain (rounded or angular). Finally, as approximately the same area was analyzed after each annealing step, we use average values for the whole mapped domain to characterize the global evolution of stored energy and grain parameters during the static heat treatment. In order to put emphasis on the evolution of large grains without filtering smaller grains from the dataset, in a few cases we weighted the averages by the area of the grains, instead of using the 95% confidence intervals of the geometric mean. All calculated parameters are provided in Supplementary Table S1a.

Results of annealing experiments are presented for selected representative samples in Figs. 2–5. The edges of the maps are cropped in order to show the same area after each annealing step. The first column of these figures displays EBSD orientation maps colored as a function of the orientation of the uniaxial compressive stress direction in the deformation experiments relative to the crystals orientation, illustrated by the inverse pole figure (IPF) in the inset. The colors red, green and blue indicate crystals, in which the compression axis is normal to the (0001), $(\bar{1}2\bar{1}0)$ and $(01\bar{1}0)$ planes, respectively. The IPF pole figures also show as contour lines the Schmid factor of the different orientations with respect to the former compression calculated using MTEX. The second column shows Mis2Mean-colored maps, where warmer colors indicate higher deviation from the mean orientation of the grain. Finally, the third column displays KAM2-colored maps, where dark bands correspond to abrupt changes in orientation, such as subgrain or kink boundaries. For more details see the caption of Fig. 2. In each annealing experiment we distinguish new and/or growing grains using a particular symbol (*e.g.*, triangle, square). Data for these grains is provided in Supplementary Table S1b.

3. Results

3.1. Microstructure of the starting material

Deformed samples have a bimodal grain size distribution, characterized by cm-size porphyroclasts with irregular shapes and serrated grain boundaries and by mm-sized strain-free recrystallized grains at the porphyroclasts boundaries or in triple junctions (Figs. 2a, 3a and 4a, 5a). Recrystallized grains tend to be equant and show less sinuous grain boundaries. The internal microstructure of the porphyroclasts is characterized by coexistence of sharp misorientation gradients, defining straight subgrain boundaries, and smooth variations in orientation between them (Fig. 2a). The subgrain boundaries are dominantly tilt boundaries (rotation axis within the boundary plane), composed by edge dislocations of the basal system, as indicated by their rotation axes subparallel to a-axes (*e.g.*, $\langle 1\bar{2}10\rangle$, $\langle \bar{1}\bar{1}20\rangle$; Fig. 6). Kink band structures, formed by a pair of tilt subgrain boundaries with opposite misorientation senses, are also commonly observed (black arrows in Fig. 2a). A close-up of the porphyroclasts reveals that in the outer part of the grains the misorientation gradients are spatially related to the sinuosity of grain boundaries, with subgrain boundaries often 'closing' a misorientated domain in a grain boundary bulge (white/blue arrow in Fig. 2a). This suggests that dynamic recrystallization in the present experiments involved grain boundary migration and nucleation (*i.e.*, bulging or migration recrystallization) and subgrain rotation. Based on the analysis of the whole specimen surface (*ca.* 9 × 9 cm, Fig. 1a) performed using the Automatic Ice Texture Analyser (AITA) immediately after the deformation experiments, the dynamically recrystallized grain fraction increases from *ca.* 3 vol% in specimens CI02 and CI06 to *ca.* 12 vol% in specimen CI18), consistently with the increase in plastic strain: 3.0%, 3.7% and 5.2%, respectively. The present deformation microstructures are comparable to those observed in other deformation studies on ice, where dominant intracrystalline slip on the basal plane (0001) is accompanied by dynamic recovery and recrystallization with nucleation preferentially occurring at grain boundaries (*e.g.*, Jacka and Maccagnan, 1984; Wilson, 1986; Montagnat and Duval, 2004; Montagnat et al., 2009, 2015; Chauve et al., 2015, 2017).

3.2. Microstructural evolution during annealing

EBSD data acquired on the same area after each annealing step highlight a common intracrystalline evolution, irrespective of the temperature at which the annealing was carried out. Figs. 2–5 illustrate the microstructural evolution in representative examples and Figs. 6–9 show the quantitative data analysis (note that annealing times are presented in a logarithmic scale).

At the sample scale, the microstructural evolution is characterized by a global decrease in the intragranular misorientations due to static recovery (reorganization and annihilation of the pre-existing dislocations) and subsequent recrystallization (creation and rearrangement of high-angle grain boundaries) (cf. Fig. 8a–b). The first annealing stages are essentially characterized by changes in the intragranular misorientation distribution (recovery) (Figs. 2b, 3b-d, 4b, 8a). Analysis of the Mis2Mean values averaged over the entire analyzed surface, which is kept constant, highlights a slight decrease in the average intragranular misorientation (Fig. 8a) indicating that annihilation processes of geometrically necessary dislocations are operating. In parallel, reorganization of geometrically necessary dislocations into low angle grain boundaries results in sharper orientation gradients across some pre-existing subgrain boundaries (Fig. 6) and creation of new ones with respect to the deformed state (compare the circled areas in Fig. 2a–b).

Nucleation, characterized by the apparition of new grains within the analyzed area, is first observed after ≥1.5 h of annealing (Fig. 8c). The nuclei are indicated by a triangle in Fig. 2c (experiment CI02Z4 [3.7/-5]) and a circle in Fig. 4c (experiment CI18Z6 [5.2/-2]). Longer annealing times are required for observing nucleation in experiments CI18Z1 [5.2/-5] (4.5 h, Fig. 3d) and CI06Z2 [3.0/-5] (5 h,

0.45 (black) to 0.05 (light gray) for the basal system in 0.05 steps. Dark gray square indicates the Schmid factor of 0.5, black square corresponds to the minimum Schmid factor of 0.3–0.4 where plastic deformation is possible. Grain boundaries and non-indexed points are displayed in black, subgrain boundaries in red. Middle column: Misorientation to the mean orientation of the grain (Mis2Mean) maps. Units are in degrees, the color coding is shown in (a). Grain boundaries and non-indexed points are shown in white. Right column: 2nd-order Kernel-averaged misorientation (KAM2) maps, which highlight sharp changes in intragranular misorientations that correspond to subgrains and kink boundaries. The units are in degrees and the color coding is shown in (a). Grain boundaries are displayed in black, non-indexed points in white. White arrows in (a) show a subgrain boundary 'closing' a misorientated domain in a grain boundary bulge. Also note the appearance of a subgrain boundary between the deformed state and the first stage of annealing (blue circles). Black arrows in the inset in (a) of the Mis2Mean-colored map shows kink bands (*i.e.*, pair of tilt subgrain boundaries with opposite misorientation senses); gray line corresponds to a misorientation profile with maximum 6° misorientation between neighboring pixels. The line in (a–c) indicate the trace of the misorientation profile presented in Fig. 6. The evolution of the grain marked by the black triangle is presented in Fig. 9. DRX indicates a non-columnar grain that has nucleated by dynamic recrystallization during the deformation experiment (*i.e.*, pre-existing nucleus). See text for further details. (For interpretation of the references to colour in this figure legend, the reader is referred to the web version of this article.)

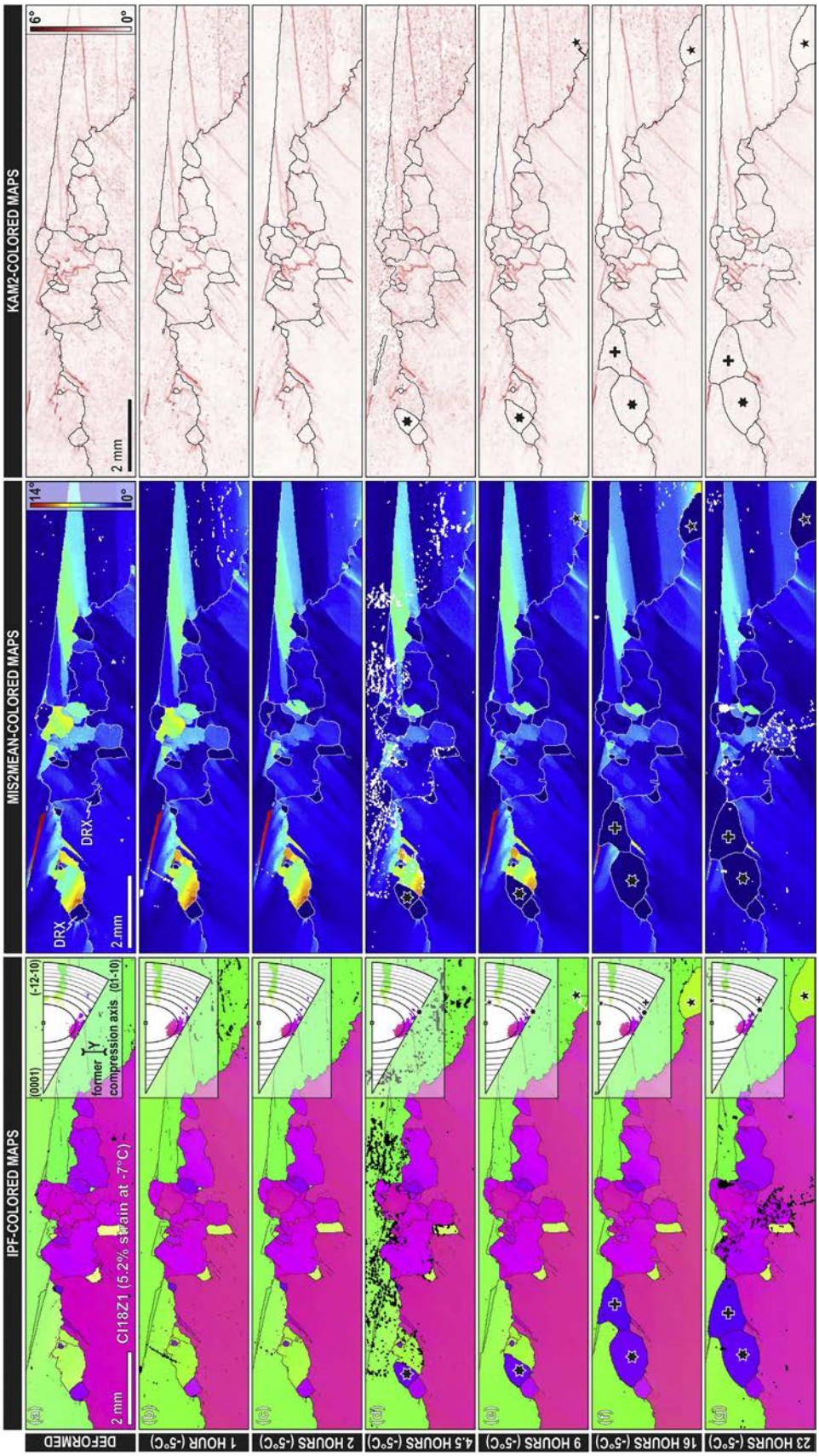

Fig. 3. Microstructural evolution during annealing for 23 h at −5 °C of the sample CI18Z1, that was pre-deformed to 5.2% macroscopic strain at −7 °C. The same area is presented in all images and the color coding of the figures is the same as for Fig. 2. The evolution of the grains marked by the black hexastar, the black pentastar and the black cross is presented in Fig. 9. DRX indicates some non-columnar grains that have nucleated by dynamic recrystallization during the deformation experiment (*i.e.*, pre-existing nucleus). (For interpretation of the references to colour in this figure legend, the reader is referred to the web version of this article.)

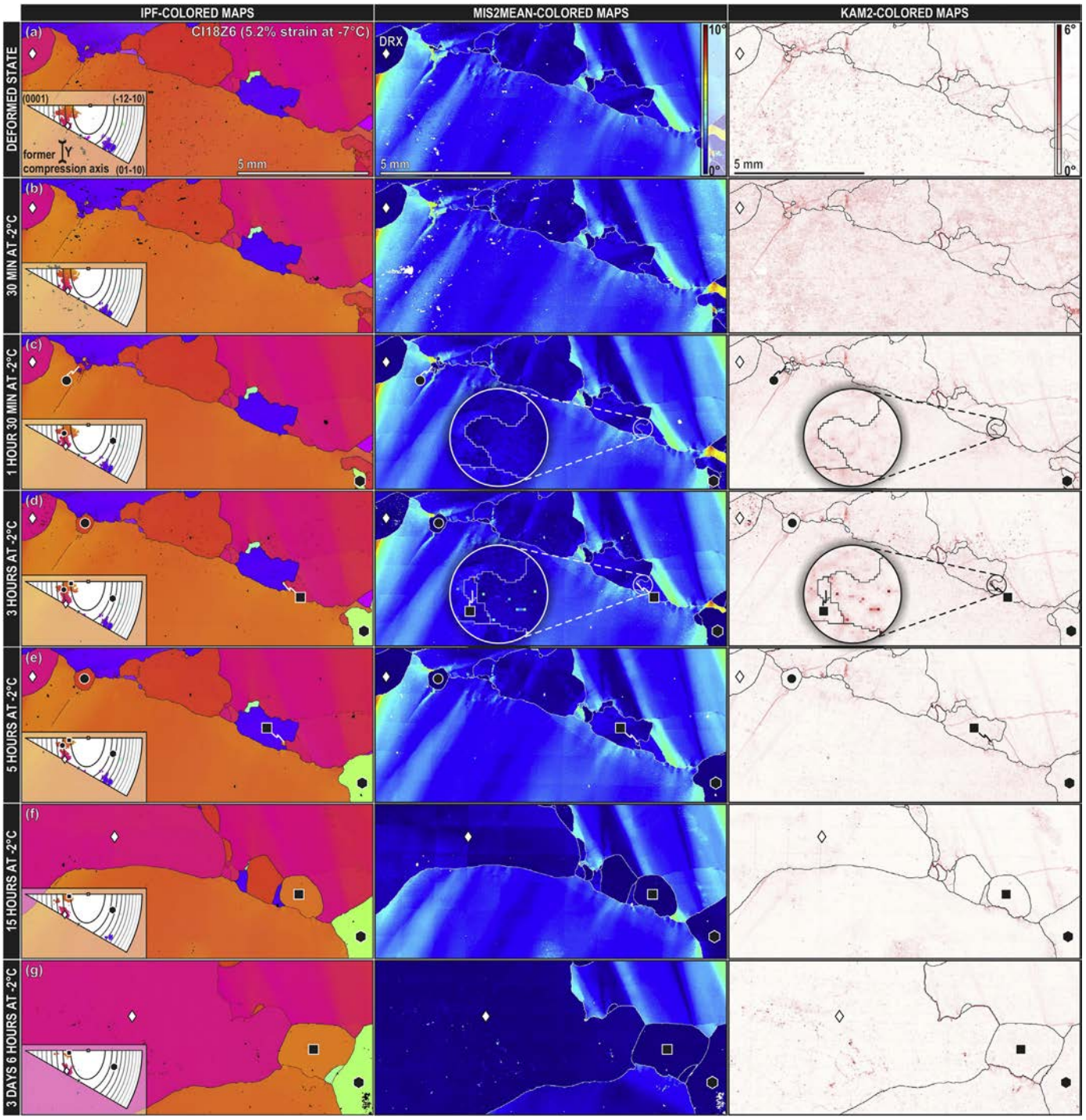

Fig. 4. Microstructural evolution during annealing for 3 days and 6 h at −2 °C of the sample CI18Z6, that was pre-deformed to 5.2% macroscopic strain at −7 °C. The same area is presented in all images and the color coding of the figure is the same as for Fig. 2. Inset in (c–d) highlights intragranular evolution prior to nucleation of the grain marked by the black square. The subtle checkerboarding visible in sections (c–f) of the figure arises from non-perfect stitching of different beam maps, which does not significantly influence the calculated values. The evolution of the grains marked by the white diamond, the black circle, the black hexagon, and the black square is presented in Fig. 9. DRX on the grain labeled by the white diamond indicates a non-columnar grain that has nucleated by dynamic recrystallization during the deformation experiment (*i.e*, pre-existing nucleus). (For interpretation of the references to colour in this figure legend, the reader is referred to the web version of this article.)

Fig. 5b). Note that we cannot exclude that nucleation started in the sample interior and was only observed at the surface after a growth interval, nor certify that the new grains in the annealing experiments were not nuclei formed during the deformation experiment, which have grown towards the surface during annealing or have been exposed to the surface during the destructive sample preparation.

The recrystallization stage disturbs the otherwise smooth evolution of the mean Mis2Mean (Fig. 8a), KAM2 (Fig. 8b), and PARIS (Fig. 8e) parameters due to the apparition and growth of new small (Fig. 9a), strain-free grains with straight grain boundary traces on the analyzed surface. The orientation of the nuclei is often similar to

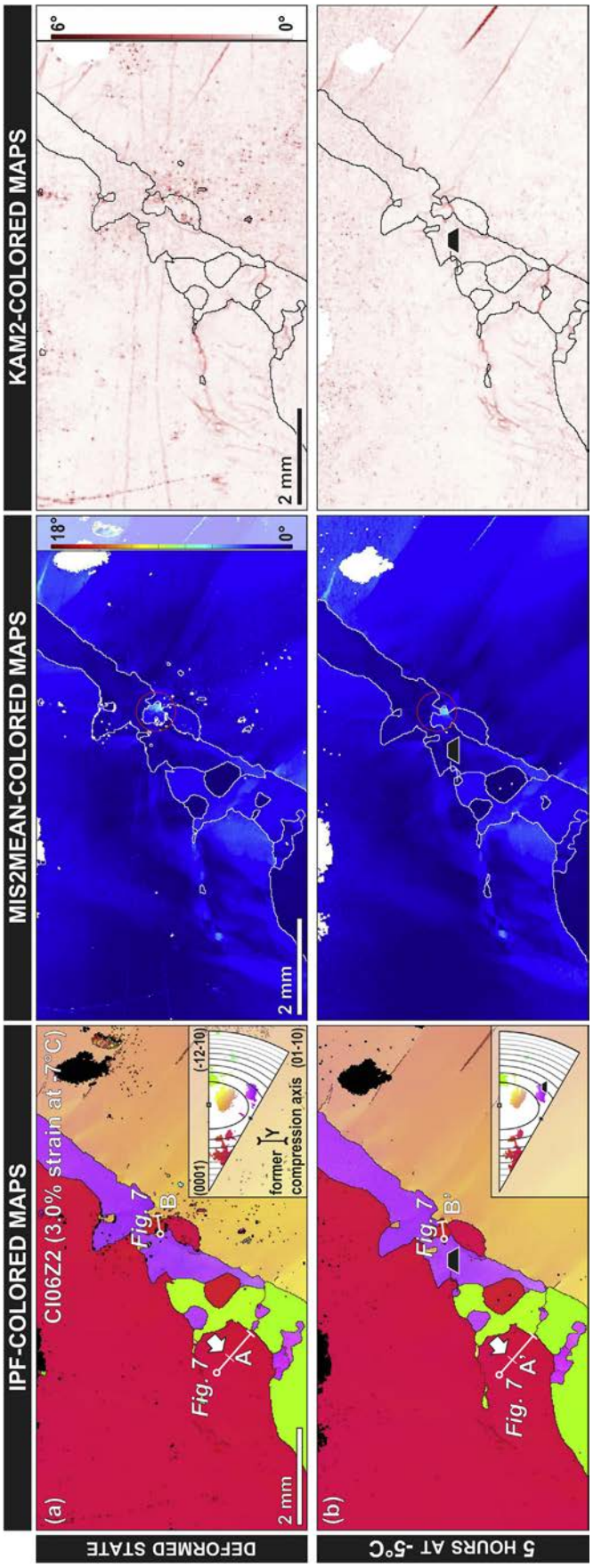

one of the neighboring pre-existing grains (cf. the orientation in the IPF of the nuclei marked by a triangle in Fig. 2, by a circle and a square in Fig. 4, and by a trapezoid in Fig. 5b). However, the orientation of two spatially close nuclei may be either very similar (*e.g.*, grains marked by the hexastar and the cross in Fig. 3) or completely different (*e.g.*, grains marked by the hexagon and the square in Fig. 4).

The annealing experiments differ by the characteristics of the nucleation site. In experiments CI02Z4 [3.7/-5] and CI18Z1 [5.2/-5], recrystallization is evidenced by appearance of new crystals within the most strongly misorientated domain in the study area (Fig. 2b–c and Fig. 3c–d, respectively). Since there were pre-existing recrystallized grains in this domain (formed during the deformation experiments), the 'new' nuclei may result from growth of a nucleus formed within the sample during the deformation experiment. In contrast, in experiment CI18Z6 [5.2/-2], nucleation mostly occurs by increase of the misorientation across subgrains within pre-existing porphyroclasts, leading to formation of new high angle boundaries (*e.g.*, grains marked by circle and square in Fig. 4c–d). The experiment CI06Z2 [3.0/-5] records an incomplete stage of this process, where subgrain rotation has not yet detached a new grain from the boundary bulging zone of the porphyroclast (circled area in Fig. 5a–b and misorientation profiles B and B′ in Fig. 7).

Following their detection, the new grains either grow fast, increasing their area by a factor up to 3 in the subsequent 2 annealing steps (*e.g.*, grains marked by the triangle in Fig. 2 and the hexagon in Fig. 4), or keep a near constant area after their appearance (*e.g.*, grains marked by hexastar in Fig. 3, and square and circle in Fig. 4). Some of these latter grains may disappear (*e.g.*, circle in Fig. 4), while others may display fast growth during the later stages of annealing (*e.g.*, hexastar in Fig. 3 and square in Fig. 4). This results in a convex upwards evolution of the area for the former and a concave upwards pattern for the latter grains, respectively (Fig. 9a). Despite its fast growth after detection, the grain marked by pentastar in Fig. 3 probably also belongs to the second group. Indeed the late detection of its nucleation suggests it might have evolved from the sample interior. Growth of nuclei formed in the previous deformation step shows more extreme evolution. In the sample CI18Z6 [5.2/-2] a pre-existing grain that nucleated during deformation (marked by white diamond in Fig. 4) shows initially very slow growth, but abnormal fast growth after 5 h of annealing (Fig. 9a).

Growing grains first consume strongly distorted parts of the deformed primary grains (Fig. 2c–f and Fig. 3d–f). Fast growth of grains (Fig. 8d) with low internal misorientations formed both during the annealing experiments or inherited from the deformed state results in acceleration in the reduction of the area-weighted misorientation (Fig. 8a) and of the frequency of subgrain boundaries (Fig. 8b). A proxy to growth rate is estimated based on the increase in area of a grain through time (Fig. 9b). Growth rates tend in average to decrease with increasing annealing time, from up to 3.0×10^{-4} mm^{2}s^{-1} in the earliest stages to $<10^{-5}$ mm^{2}s^{-1} in the late stages of textural evolution (Fig. 9b). Much faster growth rates, exceeding 5.7×10^{-4} mm^{2}s^{-1}, are nevertheless estimated for a few

Fig. 5. Microstructural evolution during annealing for 5 h at −5 °C of the sample CI06Z2, that was pre-deformed to 3.0% macroscopic strain at −7 °C. Some annealing steps have not produced any visible microstructural changes; they have been omitted from the figure for the sake of concision. The same area is presented in all images and the color coding of the figure is the same as for Fig. 2. The area circled in red shows a domain where subgrain rotation is about to isolate a new grain from a bulging zone of the porphyroclast. The misorientation profiles of A, A′ and B, B′ are shown in Fig. 7. (For interpretation of the references to colour in this figure legend, the reader is referred to the web version of this article.)

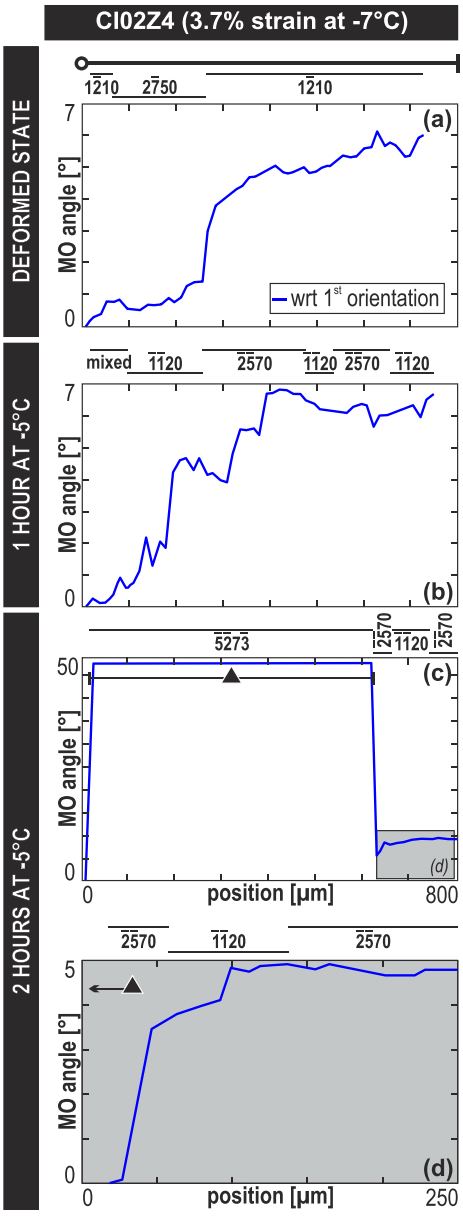

Fig. 6. Evolution of the same misorientation profile, displayed as the misorientation with respect to the first point of the profile, from (a) the deformed state, to (b) after 1 h and (c–d) after 2 h of annealing at −5 °C of the sample CI02Z4, which was pre-deformed to 3.7% macroscopic strain at −7 °C. The trace of the profile is shown in Fig. 2a–c. The most common rotation axis accommodating the misorientation in a given segment of the profile is shown above each diagram. The black triangle in (c) indicates the misorientation profile across the new grain that first appeared in Fig. 2c, and the gray shaded area shows the enlarged view of the misorientation profile in the porphyroclast close to the contact with the nucleus in (d).

grains displaying abnormal growth during the late, normal growth stages of the experiments (Fig. 9b).

Kink bands and highly misorientated tilt boundaries in the porphyroclasts are often transformed into high-angle grain boundaries of growing strain-free new grains (*e.g.*, grains marked by the triangle in Fig. 2d and the cross in Fig. 3f–g). Grain growth can be locally and temporarily pinned by the presence of such low-angle boundaries (Fig. 2d). Note that due to the destructive sample preparation (i.e., removal of a thin surface layer) before each EBSD analysis, the eventual pinning effect of thermal grooving of low-angle subgrain and high-angle grain boundary is negligible.

Microstructural changes up to about 15 h of annealing remain local. Most of the studied areas preserve the serrated grain boundaries and strong intragranular misorientations across tilt boundaries and kinks, which characterize the initial deformed microstructure (*e.g.*, Figs. 2a–f, 4a-f). The deformation microstructure is only significantly modified by grain growth in the last stage of the experiments, when effective (long-distance) grain boundary migration results in evolution of grain boundaries from serrated to polygonal (Figs. 2g, 4g and 8e) and in a marked decrease of the number of grains (Fig. 8c). Grain boundary migration also results in efficient decrease in the intragranular misorientations on the analyzed surface (Fig. 8a), as highly misorientated domains in the porphyroclasts are swept by the migrating boundaries (*e.g.*, Figs. 2g, 4f-g). In this stage, the microstructure evolves towards a polygonal aggregate of coarse, mostly undeformed crystals (Fig. 2g). Growth rates gradually decrease with annealing time for most grains except for the abnormally growing ones (marked by a white diamond in Fig. 4g). For the latter slowing down of the growth rate only occurs after extended periods of annealing (Fig. 9b).

4. Discussion

4.1. Processes and driving forces of microstructural changes during annealing

Throughout the annealing experiments the area-weighted misorientation of the analyzed surfaces gradually decreases (Fig. 8a), indicating continuous decrease of the geometrically necessary dislocation density in response to annihilation processes and, for longer annealing times, growth of strain-free recrystallized grains (Figs. 2–5). In the limited range of experimental conditions tested, the evolution rate in the initial, recovery-dominated stage is similar in all experiments (Fig. 8a), hence we find no evidence for the dependence of recovery processes on the amount of plastic strain in the deformation experiments (3.0%, 3.7%, or 5.2% strain) or the annealing temperature (−2 °C or −5 °C). This is nevertheless in agreement with data from optical fabric analysis of a statistical number of grains during static annealing of polycrystalline ice (*i.e.*, stress relaxation at the temperature of deformation following unloading), which indicate that post-deformation microstructural changes involving nucleation and grain boundary migration are not dependent on the temperature or the strain achieved in the preceding deformation (*e.g.*, Peternell et al., 2014, Peternell and Wilson, 2016; Wilson et al., 2014).

At the recrystallization stage, which is characterized by either the appearance of new grains and/or growth of pre-existing nuclei, growing crystals always contain the lowest misorientations within the mapped area and the process systematically initiates in the most misorientated domains (those that initially had high KAM2 and Mis2Mean values; Figs. 2–5). These grains evolve by movement of high-angle grain boundaries, consuming first the most distorted parts of the deformed porphyroclasts (Figs. 2–3). This observation suggests that grain boundary migration in the beginning of recrystallization is controlled by spatial variations in elastic energy associated with dislocations. This is consistent with the proposition by Wilson et al. (2014) who suggested dislocation density and not surface energy to be the rate controlling process in the early stages of static annealing of ice. Gradual decrease in grain growth rate values (Fig. 9b) is consistent to a global decrease in the elastic stored energy as annealing proceeds. Presence of subgrain and kink band boundaries slows locally and temporarily the grain boundary migration rate relative to domains with more gradual variations in orientation (Fig. 2d). This observation corroborates the lower energy of dislocation arrays, such as low-angle boundaries

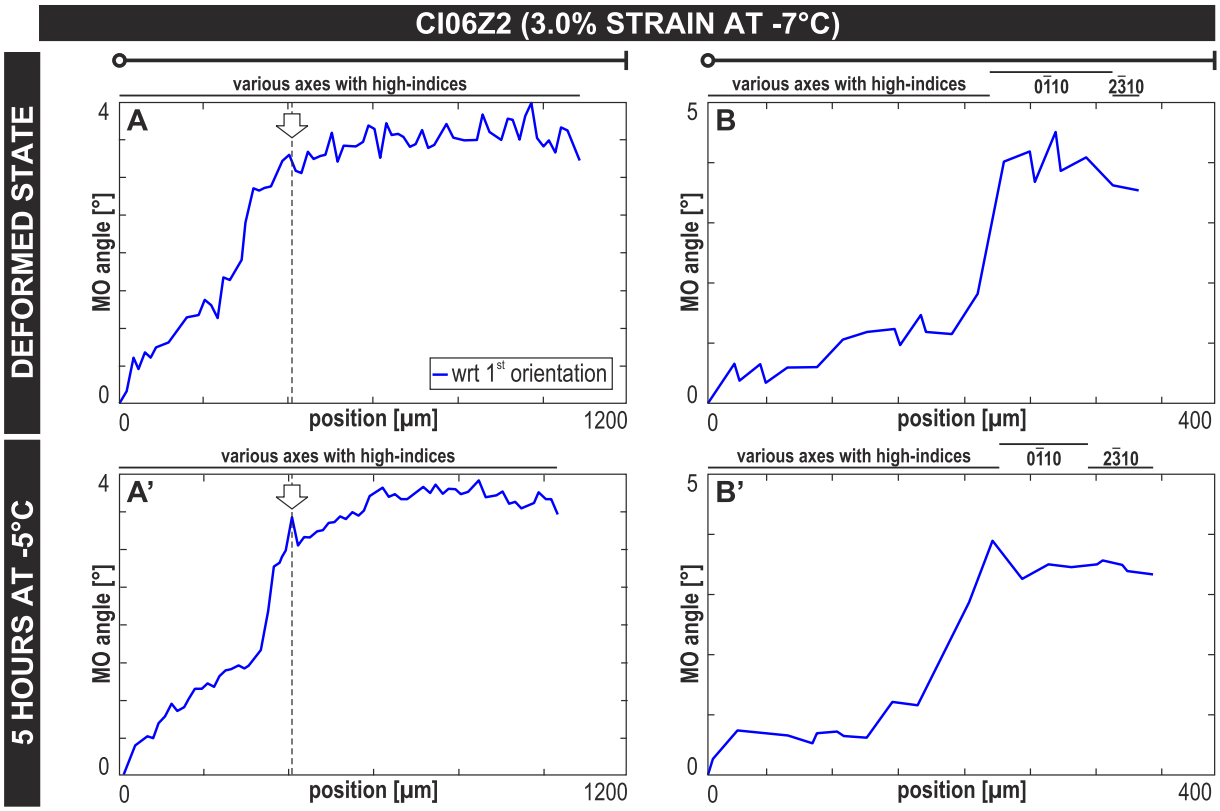

Fig. 7. Evolution of intragranular misorientations, displayed as the misorientation with respect to the first point of the profile, along two representative profiles during annealing for 5 h at −5 °C of the sample CI06Z2, which was pre-deformed to 3.0% macroscopic strain at −7 °C. Profiles A and B correspond to the deformed state, whereas A′ and B′ are taken at approximately at the same position after 5 h of annealing. The traces of the profiles are shown in Fig. 5. The most common rotation axes accommodating misorientations in a given segment of the profile is shown above each diagram. White arrow in profile A and A′ indicates a subgrain boundary that increased misorientation during the preceding recovery stage (see Fig. 5 for location). See text for further details.

(*e.g.*, Humphreys and Hatherly, 2004).

The limited number of grains in our samples does not allow for a statistical analysis of grain morphology (*e.g.*, Peternell et al., 2014, Peternell and Wilson, 2016; Wilson et al., 2014), but during thermal annealing we observe increase in grain size (Fig. 8d), decrease in the tortuosity of grain boundaries (*i.e.*, decrease of the PARIS values; Fig. 8e), and an evolution of triple junctions towards equilibrium angles of 120° (Figs. 2–4). These observations suggest that reduction of grain boundary surface area (and energy) is another important driving force for the evolution of the microstructures close to the melting temperature and that it becomes predominant in the evolved stages of annealing (>15 h). This conclusion is consistent with the common sense one, recalled by Wilson et al. (2014), that grain-boundary energy has an increasing role with time in static annealing. The lower values of grain boundary energy relative to the elastic energy associated with dislocations (*e.g.*, Humphreys and Hatherly, 2004) may explain the observed decrease in the grain boundary migration rates.

4.2. Nucleation processes

In the present study the actual process of nucleation cannot be directly observed. Irrespective of the annealing conditions and of the pre-existing deformation, new nuclei are only detected after a minimum incubation period of 1.5–2 h (Figs. 2c, 3d 4c 5b and 8c). Similar incubation periods, sometimes lasting up to 3 h, were observed in static annealing experiments in metallic alloys (*e.g.*, Humphreys and Hatherly, 2004) and in polycrystalline ice (*e.g.*, Peternell et al., 2014, Peternell and Wilson, 2016; Wilson et al., 2014). Humphreys and Hatherly (2004) proposed that grain growth during thermal annealing may occur from invisible, but pre-existing dislocation cells that formed during the deformation, hence the incubation period may correspond only to the first detection of these new small grains, which primarily depends on the applied analytical technique (in our case the step size of the overview maps and the angular resolution of EBSD). Therefore nuclei which give rise to the new recrystallized grains may not have formed *sensu stricto* during the annealing, but perhaps represent small volumes which pre-exist in the deformed microstructure and become visible due to grain growth (*e.g.*, Humphreys and Hatherly, 2004; Rios et al., 2005; Wilson et al., 2014). It is noteworthy that the samples deformed to 3% were the last to nucleate new grains (Figs. 5 and 8c). This suggests that higher strain levels might have resulted in a higher proportion of local structures, such as dislocation cells, favoring nucleation. Indeed, under the deformation conditions of the present experiments, a steady-state microstructure is only achieved for strains >10% (Jacka and Jun 1994; Montagnat et al., 2015).

Analysis of the crystallographic orientation of the nuclei relative to the neighboring grains highlights two types of relation. Most nuclei have orientations close to at least one of the neighboring deformed grains (Figs. 2–5). In some cases, such as the nucleus marked by the circle in Fig. 4, there is a clear evolution from a bulge displaying a high misorientation gradient relative to the parent towards a new grain, suggesting that nucleation occurred by a mixed process involving bulging and increase of the misorientation across an existing subgrain boundary. The same process is caught in the act in Fig. 5 (cf. circled areas and the corresponding

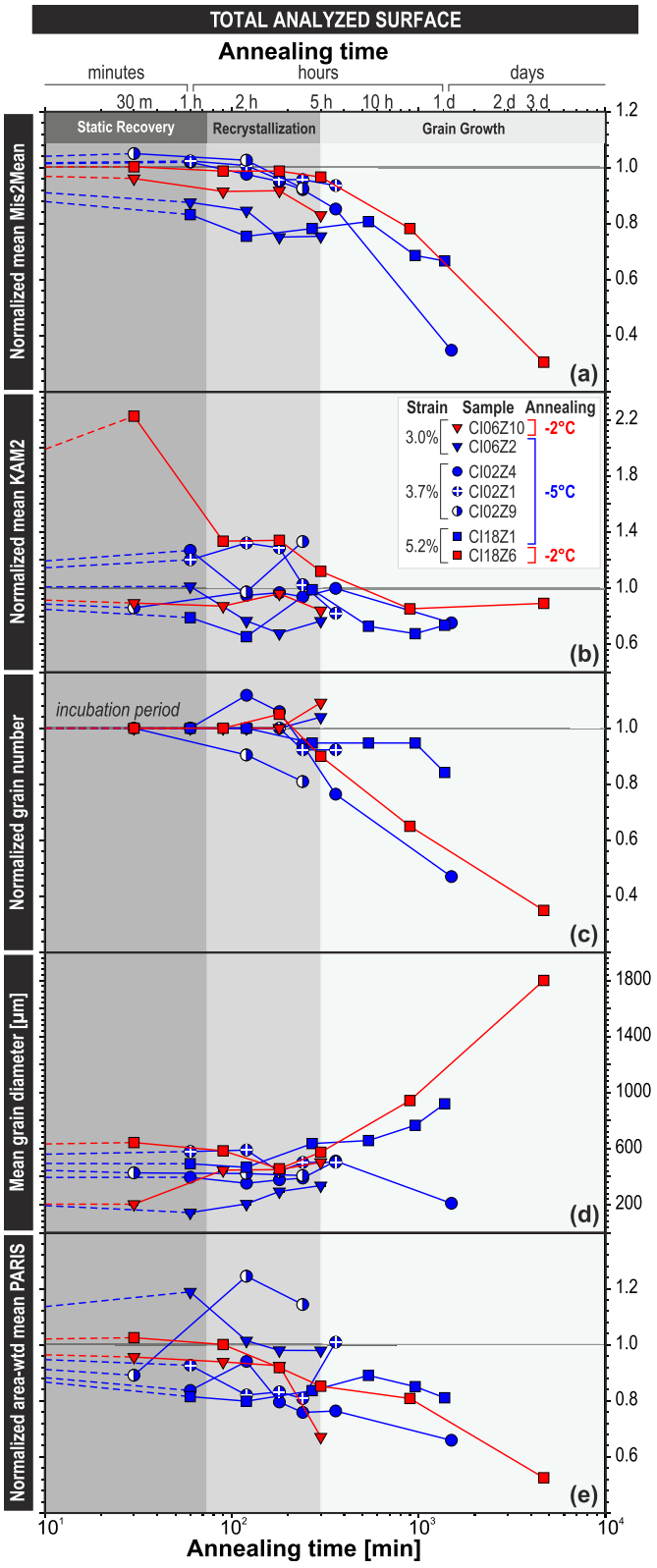

Fig. 8. Evolution of the microstructure over the total analyzed surface in all experimental runs. Values in each annealing step are normalized to the corresponding value in the deformed state, except for (d). Dashed lines before the first annealing step indicate early evolution of the samples with values corresponding to the deformed state plotted at t = 10^{-5} min and lines cropped at t = 10 min. Data is presented in Supplementary Table S1a. (a) Mean misorientation to the mean orientation (Mis2Mean). (b) Mean second nearest-neighbor kernel average misorientation (KAM2). (c) Number of grains. (d) Mean grain diameter. (e) Area-weighted Percentile Average Relative Indented Surface (PARIS) factor.

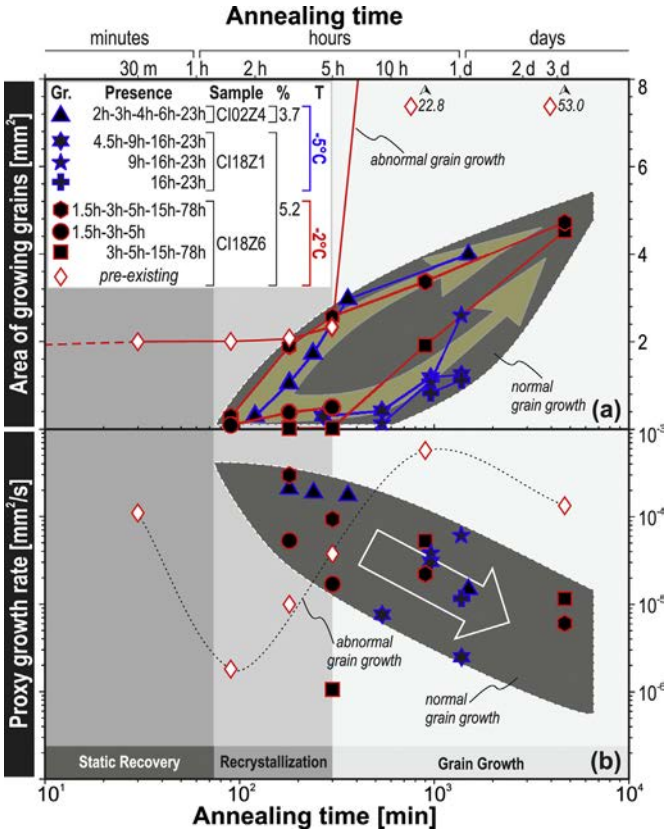

Fig. 9. Evolution of selected grains that nucleated and/or grew during the annealing experiments. The location of the grains is presented in Figs. 2–4 using the same symbols. The grain indicated by the white diamond nucleated during the deformation experiments (pre-existing nucleus). Dark gray field encompasses the grains that show normal grain growth. (a) Area [in mm^2] of growing grains in representative samples. The arrows indicate convex upwards (top) and concave upwards (bottom) evolution trends. See text for more details. (b) Proxy to growth rate [in mm^2s^{-1}] defined as the difference in area of a given grain divided by the time between two subsequent annealing steps. Data is presented in Supplementary Table S1b.

misorientation profile in Fig. 7). This evolution has also been observed during dynamic recrystallization of ice (Chauve et al., 2017), indicating that subgrain rotation and bulging are not competing processes, but cooperate for more efficient nucleation. In other cases, the nuclei are not in direct contact with the inferred parent grain (grains marked by triangle in Fig. 2, star and cross in Fig. 3, as well as square in Fig. 4), suggesting that they grew from nuclei formed below the surface, probably formed by similar processes. Finally, some of the observed nuclei were detected close to the limits of the mapped area, that hinders effective analysis of their orientation relation with possible parent grains, which might be outside the mapped area. This is the case of the nucleus marked by a hexagon in Fig. 4.

The analysis of the nucleation observations in the present experiments suggests that misorientation has to be distributed over a certain volume for a successful nucleation. Sharp misorientations accumulated along tilt- or kink-boundaries (see the sharp orientation changes in Figs. 2–3) do not serve as nucleation sites during annealing. This observation is consistent with low stored energy of these dislocation arrangements. Nucleation sites in our experiments are few (1–2 per map; Figs. 2–5). This may be due to the relatively small area and the limited number of grains (<25 grains, Fig. 1a) analyzed in each experiment. Alternatively, the high temperature of deformation (0.97 T_m) coupled to the relatively small plastic strain (<5.2%) may have limited the storage of elastic energy

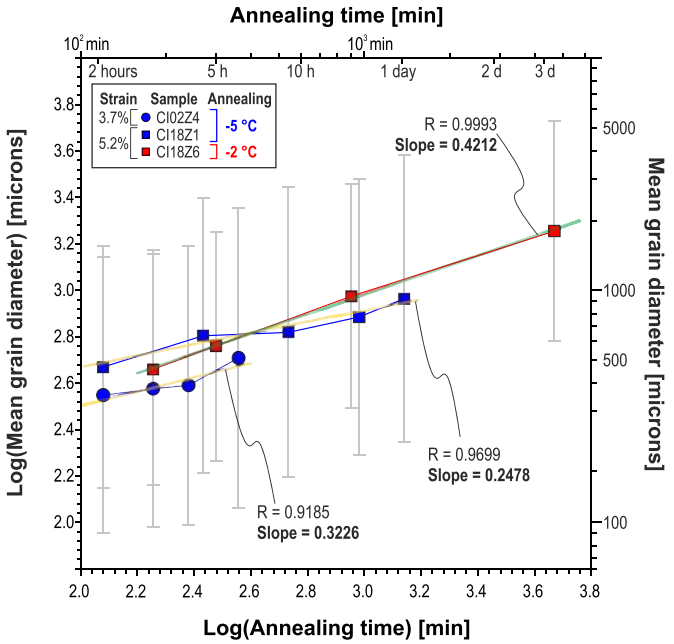

Fig. 10. Calculated grain growth kinetics based on the adjustment of the evolution of the mean equivalent grain diameters between 2 and 78 h of annealing for the experiments presented in Figs. 2–4 using the parabolic growth law of Humphreys and Hatherly (2004). Note that units are in microns and minutes for grain size and annealing time, respectively. For sample CI02Z4 [3.7/-5] only the data with positive slope has been considered. The slopes of the linear least squares fitted lines provide the grain growth exponent (slope = 1/n value). See text for further details.

in the crystalline structure during deformation which was further reduced during unloading of the creep experiments (Duval et al., 1983). The delayed microstructural evolution (up to 4.5–5 h, Figs. 5 and 8c) in samples deformed to the lowest strains (3.0%) seems to support this proposition.

4.3. Grain growth kinetics

In polycrystalline materials without excessive amount of second phase particles, when the main driving force for grain growth is the reduction of the total grain boundary energy, grain growth kinetics should follow a parabolic law according to the equation

$$D^n - D_0^n = K\,t, \quad (1)$$

which reduces to

$$D = K'\,t^{1/n} \text{ if } D^n >> D_0^n, \quad (2)$$

where D_0 is the initial mean grain size, D is the mean grain size at time t, n is the grain growth exponent, and K′ is a temperature-dependent grain growth constant (cf. review in Humphreys and Hatherly, 2004). Experimental studies for metals and ceramics report that the grain growth exponent can vary from 2 to 20 as a function of impurity content and temperature, with lowest values being obtained at high homologous temperatures in the highest purity materials (see Humphreys and Hatherly, 2004 for a compilation). Indeed, normal grain growth in ideal materials with isotropic boundary energy should be characterized by grain growth exponent of 2 (Burke and Turnbull, 1952).

In Fig. 10, we display the fit of the data for the annealing experiments presented in Figs. 2–4 between 2 and 78 h (steady-state grain growth) by Equation (2). This fit defines grain growth exponents of 2.4 (experiment of CI18Z6 [5.2/-2]; Fig. 4), 3.1 (experiment CI02Z4 [3.7/-5]; Fig. 2) and 4.0 (experiment CI18Z1 [5.2/-5]; Fig. 3). Note that the slope of the trend lines fitted on grain growth data equals to 1/n. These values are consistent with those measured in polycrystalline ice made of double distilled water (3.3; *e.g.*, Jellinek and Gouda, 1969) and in high purity metals and ceramics (with impurity levels no more than a few ppm) close to their melting temperature (ranging from 2 to 4 with an average of 2.4 ± 0.4; Humphreys and Hatherly, 2004). They are also consistent with the data from Higgins (1974), which shows that at homologous temperatures ≥0.9 T_m the grain growth exponent is typically in the range of n = 2–5. The observed grain growth exponents are coherent with the facts that the present samples are synthetic polycrystalline columnar ice-I_h made from ultra pure water and that the annealing was performed at homologous temperatures of 0.98–0.99. Although the variation is probably within the error of measurement, a lower value of grain growth exponent is observed for the annealing at higher temperature (2.4 at −2 °C vs. 3.1–4.0 at −5 °C).

The subtle deviation of the observed grain growth exponents from the theoretical value of 2 (Burke and Turnbull, 1952) might be explained by the presence of invisibly small air bubbles entrapped during crystallization, that would slow down grain growth (*e.g.*, Roessiger et al., 2014). An alternative explanation could be the influence of subgrain boundaries and kink bands, which tend to pin the moving grain boundaries during the annealing experiments (Fig. 2d).

4.4. Significance of the experimental observations for natural systems

Static recrystallization is considered to have limited importance in glaciers and ice sheets, because of the almost continuous deformation of most ice bodies, in particular, the glaciers. In addition, the time scale for temperature changes in a glacier is very long compared to the recrystallization time scales (Schulson and Duval., 2009). However, our data show that only a minor increase in temperature with respect to that of the deformation (ΔT = 2–5 °C; Table 1) in moderately deformed (<5.2% strain) polycrystalline ice may result in significant microstructural evolution in just a matter of days. The present stepwise experiments demonstrate that annealing is cumulative, as textural changes keep developing in the same areas despite the extreme temperature differences (>100 °C) seen by the samples between two annealing cycles (Fig. 1b). This suggests that short yet repeated heating periods may have a comparable impact on the microstructure to long, extended heating events. Therefore, if the conditions for efficient static recrystallization are met at least locally, annealing may influence the long-term evolution of the warmer levels of deep polar ice sheets (*e.g.*, Price et al., 2002) and that of the surface layers of temperate glaciers (down to about hundred meters), where important temperature variations occur (Lüthi and Funk, 2001; Cuffey and Paterson, 2010). Note, that the present observations cannot not be extrapolated to ice bodies, because grain boundary mobility in ice-I_h drops markedly below −10 °C (Duval and Castelnau, 1995).

The present experiments also show that intragranular recovery proceeds from the earliest stages of annealing without producing clear changes to the pre-annealing texture (compare Fig. 6a–b and Fig. 8a–b with Figs. 2–5). Extrapolating this observation to the Earth's interior implies that caution is needed when interpreting present day intragranular misorientations as recording the dislocation arrangements directly associated with the deformation. Dislocation arrangements in lower crustal and mantle rocks are likely to have been changed since the cessation of deformation even if the microstructure shows no obvious sign of annealing

phenomena.

5. Conclusions

Stepwise static annealing experiments and coupled EBSD analyses of laboratory-made, pre-deformed polycrystalline columnar ice show that recovery starts at the earliest stages of annealing. This recovery results in the decrease of intragranular misorientations and modifies the misorientations across some subgrain boundaries, but it does not significantly change the visible microstructure. The evolution in this stage is similar for all samples, irrespective of the degree of preceding deformation (3.0–5.2% strain at −7 °C), or the temperature of annealing (−2 °C or −5 °C). The first new nuclei are observed after an incubation period ≥1.5 h, usually within regions with strong, but gradual misorientation gradients. Nucleation at sharp misorientation gradients has not been observed. Subsequent grain growth preferentially proceeds at the expenses of domains with initially high intragranular misorientations, particularly those that are characterized by gradual misorientations. High-angle grain boundaries and deformation-induced microstructures (subgrain boundaries and kink bands) are stable features, which tend to pin grain growth. This observation corroborates the low energy of dislocation arrays, such as low-angle tilt boundaries in ice-I_h. Based on these observations, we suggest that reduction of elastic energy associated with dislocations is the main driving force controlling both the early recovery (<2 h) and the earliest stages of static recrystallization (2–5 h). Given that serrated grain boundaries become more rectilinear over time, we propose that reduction of grain boundary surface area (and energy) is another important driving force for the evolution of the microstructures and that it becomes predominant in the evolved stages of annealing (>15 h). The observed grain growth kinetics are consistent with a parabolic growth law characterized by grain growth exponents in the range of 2.4–4.0.

Acknowledgements

We acknowledge the reviews by Lars Hansen and Mark Peternell, as well as the editorial work of Cees W. Passchier. Research leading to these results was funded by the European Union Framework Programme 7 (EU-FP7) Marie Curie postdoctoral grant to K.H. [grant number PIEF-GA-2012-327226]. Financial contribution from the French 'Agence Nationale de la Recherche' is also acknowledged [grant number #ANR-13-BS09-0001-01; project DREAM]. T.C. and M.M. acknowledge support from the Grenoble Institute of Technology (Grenoble INP) and the Université Joseph Fourier grant AGIR 2012.

Appendix A. Supplementary data

Supplementary data related to this article can be found at http://dx.doi.org/10.1016/j.jsg.2017.05.001.

References

Ashby, M.F., 1970. The deformation of plastically non-homogeneous materials. Philos. Mag. 21, 399–424.

Bachmann, F., Hielscher, R., Schaeben, H., 2010. Texture analysis with MTEX - free and open source software toolbox. Solid State Phenom. 160, 63–68.

Bestmann, M., Piazolo, S., Spiers, C.J., Prior, D.J., 2005. Microstructural evolution during initial stages of static recovery and recrystallization: new insights from in-situ heating experiments combined with electron backscatter diffraction analysis. J. Struct. Geol. 27, 447–457.

Borthwick, V.E., Piazolo, S., 2010. Post-deformational annealing at the subgrain scale: temperature dependent behaviour revealed by in-situ heating experiments on deformed single crystal halite. J. Struct. Geol. 32, 982–996.

Borthwick, V.E., Schmidt, S., Piazolo, S., Gundlach, C., 2012. Quantification of mineral behavior in four dimensions: grain boundary and substructure dynamics in salt. Geochem. Geophys. Geosystems 13 n/a-n/a.

Burke, J.E., Turnbull, D., 1952. Recrystallization and grain growth. Prog. Metal Phys. 3, 220–292.

Chauve, T., Montagnat, M., Vacher, P., 2015. Strain field evolution during dynamic recrystallization nucleation; A case study on ice. Acta Mater. 101, 116–124.

Chauve, T., Montagnat, M., Barou, F., Hidas, K., Tommasi, A., Mainprice, D., 2017. Investigation of Nucleation Processes during Dynamic Recrystallization of Ice Using Cryo-EBSD. Philosophical Transactions of the Royal Society A: Mathematical Physical and Engineering Sciences, p. 375.

Cuffey, K.M., Paterson, W.S.B., 2010. The Physics of Glaciers. Elsevier.

Duval, P., Ashby, M.F., Anderman, I., 1983. Rate-controlling processes in the creep of polycrystalline ice. J. Phys. Chem. 87, 4066–4074.

Duval, P., Castelnau, O., 1995. Dynamic recrystallization of ice in polar ice sheets. J. Phys. IV 05. C3–197-C193-205.

Gottstein, G., Shvindlerman, L.S., 1992. On the true dependence of grain boundary migration rate on driving force. Scripta Metall. Mater. 27, 1521–1526.

Grennerat, F., Montagnat, M., Castelnau, O., Vacher, P., Moulinec, H., Suquet, P., Duval, P., 2012. Experimental characterization of the intragranular strain field in columnar ice during transient creep. Acta Mater. 60, 3655–3666.

Higgins, G.T., 1974. Grain-boundary migration and grain growth. Metal Sci. 8, 143–150.

Humphreys, F.J., Ferry, M., Brough, I., Johnson, C.P., 1996. Combined in situ SEM annealing and EBSD of deformed materials. Textures Microstruct. 26–27, 281–301.

Humphreys, J., Hatherly, M., 2004. Recrystallization and Related Annealing Phenomena. Elsevier, Oxford.

Jacka, T.H., 1984. Laboratory studies on relationships between ice crystal size and flow rate. Cold Regions Sci. Technol. 10, 31–42.

Jacka, T.H., Jun, L., 1994. The steady-state crystal size of deforming ice. Ann. Glaciol. 20, 13–18.

Jacka, T.H., Maccagnan, M., 1984. Ice crystallographic and strain rate changes with strain in compression and extension. Cold Regions Sci. Technol. 8, 269–286.

Jellinek, H.H.G., Gouda, V.K., 1969. Grain growth in polycrystalline ice. Phys. Status Solidi 31, 413–423.

Lüthi, M.P., Funk, M., 2001. Modelling heat flow in a cold, high-altitude glacier: interpretation of measurements from Colle Gnifetti, Swiss Alps. J. Glaciol. 47, 314–324.

McMahon, C., Soe, B., Loeb, A., Vemulkar, A., Ferry, M., Bassman, L., 2013. Boundary identification in EBSD data with a generalization of fast multiscale clustering. Ultramicroscopy 133, 16–25.

Montagnat, M., Blackford, J.R., Piazolo, S., Arnaud, L., Lebensohn, R.A., 2011. Measurements and full-field predictions of deformation heterogeneities in ice. Earth Planet. Sci. Lett. 305, 153–160.

Montagnat, M., Chauve, T., Barou, F., Tommasi, A., Beausir, B., Fressengeas, C., 2015. Analysis of dynamic recrystallization of ice from EBSD orientation mapping. Front. Earth Sci. 3.

Montagnat, M., Durand, G., Duval, P., 2009. Recrystallization processes in granular ice. Low Temp. Sci. 68, 81–90.

Montagnat, M., Duval, P., 2004. Dislocations in ice and deformation mechanisms: from single crystals to polar ice. Defect Diffus. Forum 229, 43–54.

Nakamichi, H., Humphreys, F.J., Brough, I., 2008. Recrystallization phenomena in an IF steel observed by in situ EBSD experiments. J. Microsc. 230, 464–471.

Ohotomo, M., 1985. Crystallographic orientation of the recrystallized grain grown in the deformed single crystal of ice. Contrib. Inst. Low Temp. Sci. A34, 1–21.

Panozzo, R., Hurlimann, H., 1983. A simple method for the quantitative discrimination of convex and convex-concave lines. Microsc. Acta 87, 169–176.

Peternell, M., Dierckx, M., Wilson, C.J.L., Piazolo, S., 2014. Quantification of the microstructural evolution of polycrystalline fabrics using FAME: application to in situ deformation of ice. J. Struct. Geol. 61, 109–122.

Peternell, M., Wilson, C.J.L., 2016. Effect of strain rate cycling on microstructures and crystallographic preferred orientation during high-temperature creep. Geology 44, 279–282.

Piazolo, S., Bestmann, M., Prior, D.J., Spiers, C.J., 2006. Temperature dependent grain boundary migration in deformed-then-annealed material: observations from experimentally deformed synthetic rocksalt. Tectonophysics 427, 55–71.

Piazolo, S., Montagnat, M., Blackford, J.R., 2008. Sub-structure characterization of experimentally and naturally deformed ice using cryo-EBSD. J. Microsc. 230, 509–519.

Plé, O., Meyssonnier, J., 1997. Preparation and preliminary study of structure-controlled S2 columnar ice. J. Phys. Chem. B 101, 6118–6122.

Price, P.B., Nagornov, O.V., Bay, R., Chirkin, D., He, Y., Miocinovic, P., Richards, A., Woschnagg, K., Koci, B., Zagorodnov, V., 2002. Temperature profile for glacial ice at the South Pole: implications for life in a nearby subglacial lake. Proc. Natl. Acad. Sci. 99, 7844–7847.

Rigsby, G.P., 1960. Crystal orientation in glacier and experimentally deformed ice. J. Glaciol. 3, 589–606.

Rios, P.R., Siciliano Jr., F., Sandim, H.R.Z., Plaut, R.L., Padilha, A.F., 2005. Nucleation and growth during recrystallization. Mater. Res. 8, 225–238.

Roessiger, J., Bons, P.D., Faria, S.H., 2014. Influence of bubbles on grain growth in ice. J. Struct. Geol. 61, 123–132.

Schulson, E.M., Duval, P., 2009. Creep and Fracture of Ice. Cambridge University Press.

Steinemann, S., 1958. Experimentelle Untersuchungen zur Plastizitat von Eis. Beitrage zur Geol. Schweiz - Hydrol. 10, 4–72.

Weikusat, I., De Winter, D.A.M., Pennock, G.M., Hayles, M.,

Schneijdenberg, C.T.W.M., Drury, M.R., 2011. Cryogenic EBSD on ice: preserving a stable surface in a low pressure SEM. J. Microsc. 242, 295–310.
Wilson, C.J.L., 1982. Texture and grain growth during the annealing of ice. Textures Microstruct. 5, 19–31.
Wilson, C.J.L., 1986. Deformation Induced Recrystallization of Ice: the Application of in Situ Experiments, Mineral and Rock Deformation: Laboratory Studies: the Paterson Volume. American Geophysical Union, pp. 213–232.
Wilson, C.J.L., Peternell, M., Piazolo, S., Luzin, V., 2014. Microstructure and fabric development in ice: lessons learned from in situ experiments and implications for understanding rock evolution. J. Struct. Geol. 61, 50–77.
Wright, S.I., Nowell, M.M., Field, D.P., 2011. A review of strain analysis using electron backscatter diffraction. Microsc. Microanal. Off. J. Micros. Society Am. Microbeam Anal. Society Microsc. Soc. Can. 17, 316–329.